2D Hetero-nanostructural Reduced-CuNiFe-Oxides with Self-produced H_2O_2 Fenton-like Photocatalysis for Tetracycline Degradation

Lin Fu[a,‡], Dandan Wu[b,‡], Ming Wen[a,*], Yuanzheng Zhu[c], Qingsheng Wu[a], Tao Zhou[d], Yongqing Fu[e]

Fenton-like photocatalysis, an advanced oxidation techonolgy, has been considered as a promising solution to degrade tetracycline antibiotics (TCs) pollutant, but still remains challenges to achieve a high degradation efficiency in environmental friendly way. Herein, cluster structures assembled by 2D nanosheets of reduced CuNiFe mixed-metal-oxides (re-CuNiFe-MMOs) have been synthesized through a combined hydrothermal and polyols-solvothermal reduction process. The synergistic effect induced by multiphases of MMOs and CuNi alloy endows the obtained re-CuNiFe-MMOs with superior Fenton-like photocatalytic activity for the degradation of TCs without using any additional oxidants, which is mainly attributed to the generated reactive oxygen species (the dominant $^{\bullet}O_2^-$) under the visible light based on synergy of multiphases. Degradation rate of TC reaches 100% in just 4 minutes with a constant reaction rate of 1.65 min^{-1}, and this can be maintained at 95.5% after 12 cycles. This study provides an environmentally friendly approach for treatments of antibiotic pollutions directly using the visible light.

1. Introduction

Tetracycline antibiotics (TCs) are widely applied to treat human and animal diseases due to their low cost and excellent antibacterial activities.[1] However, owing to their long half-life and poor biodegradation characteristics, a large amount of TCs residues are accumulated in the water sources, which seriously threatens the ecosystem and the health of human beings and animals.[2-4] Therefore, it is crucial to explore a cheap, safe and effective way to degrade TCs contaminants.

Advanced oxidation process (AOP) has been considered as one of the promising ways to degrade various types of organic pollutants (e.g. antibiotics) into low- or non-toxic small molecules in water, because it can generate various types of reactive oxygen species (ROSs) to accelerate the degradation reactions.[5] Recently, Fenton and photocatalysis methods become popular for the degradation of toxic contaminants.[6] Unfortunately, effectiveness of Fenton processes is strongly dependent on the pH value of the solutions. They often require a large amount of oxidizing agents such as hydrogen peroxide (H_2O_2) or persulfate, and also produce massive amounts of iron sledges which is difficult separated from catalyst afterwards.[7] On the other hand, although the photocatalysis can use ROSs produced by photogenerated electrons (e^-) and holes (h^+) to oxidize and degrade antibiotics,[8] it is limited by poor visible light utilization and severe recombination of e^- and h^+.[9] Photocatalysts with multiphases of metal and semiconductor are expected to solve the above-mentioned problems. They can be readily modified to adjust their bandgaps, efficiently transfer interfacial charges, and significantly reduce recombination of photogenerated e^- and h^+, therefore, have now become one of the effective ways to improve the degradation efficiency.[10] Transition metals (such as Cu, Fe, Co, etc.) can produce different valence states to form multiphasees interfaces (e.g., biochar modified $CuFeO_2$, $CuFe_2O_4/Bi_2O_3$, and $CuCo_2S_4$, etc.).[11-13] In addition, efficient transfer of e^- or h^+ greatly promotes the production of active free radicals, enhancing the catalytic degradation performance.[14,15] If the electrons and abundant H_2O_2 produced by photocatalysis can be directly used in the Fenton-like process, it will avoid the uses of oxidants and simultaneously promote effective separation of photogenerated e^-/h^+ pairs. Hence, the synergy of photocatalysis and Fenton-like effects can be applied to generate highly reactive free radicals in oxidantless, thus improving the efficiency of oxidative degradation.

Furthermore, microstructure of the catalyst is one of the important factors to influence its photocatalytic performance.[16] Two-dimensional (2D) ultrathin heterostructures have large photosensitive surfaces, which can shorten the carriers' migration distance, provide multiple surface reaction sites, and reduce the energy barrier for reactions, all of which are favorable for effective migration and transfer of photogenerated carriers to achieve superior catalytic performance.[17-19] It is worth mentioning that the nanosheet-assembled clusters not only have the features of 2D ultrathin heterostructures, but also provide stable structures to prevent severe agglomeration of nanosheets.[20-23] Therefore, these 2D ultrathin heterostructures based Fenton-like photocatalysts containing multiphases of metals and semiconductors are effective to solve the problem of antibiotic contamination in an environment friendly manner.

In this study, a cluster structure assembled by 2D nanosheets of reduced CuNiFe mixed-metal-oxides (re-CuNiFe-MMOs) (Fig. 1) has been successfully synthesized through a combined hydrothermal and polyols solvothermal reduction (HPSR) process. When used as

the Fenton-like photocatalyst but without adding H_2O_2, this re-CuNiFe-MMOs nanosheet can achieve an outstanding degradation efficiency on the TCs, including tetracycline (TC), chlortetracycline (CTC) and oxytetracycline (OTC). The excellent performance has been identified due to the following reasons. 1) The cluster structure assembled by re-CuNiFe-MMOs nanosheets can offer a larger specific surface area and expose more active sites, which are beneficial to the catalytic degradation process; 2) The re-CuNiFe-MMOs with multiple-nanophases (including CuNi, Cu_2O, CuO, FeO and NiO) can adjust the band-gaps and facilitate effective electron transfer, both of which improve the utilization of visible light; 3) The synergy of photocatalysis and Fenton-like effect not only has a high oxidative degradation ability for TCs, but also avoids the uses of strong oxidants in the Fenton-like process, which can be produced by the photocatalysis process and hydroxyl oxidation on the surface of the catalyst; 4) A large number of defects (e.g., oxygen vacancies (OVs)) formed by *in situ* reduction of CuNiFe-MMOs can react with oxygen molecules and provide more numbers of ROSs, thus accelerating the degradation rate of TCs. Based on the above analysis, the synergetic effects among CuNi-nanophase, FeO and Cu mixture oxides can effectively enhance Fenton-like photocatalysis toward degradation of TCs without the need of oxidants. Therefore, this study is of great significant to develop an environment friendly approach for high efficiency treatment of TCs pollution in oxidantless.

2. Experimental

2.1. Synthesis of re-CuNiFe-MMOs

Chemical reagents used in the experiments are described in the electronic supplementary information Text S1 (Supporting Information). The heterostructure clusters assembled by re-CuNiFe-MMOs nanosheets were fabricated through the HPSR method based on the following procedures. $Cu(NO_3)_2{\cdot}3H_2O$ (4 mL, 10 mM), $Fe(NO_3)_3{\cdot}9H_2O$ (4 mL, 10 mM), and $Ni(NO_3)_2{\cdot}6H_2O$ (5 mL, 20 mM) were mixed firstly, then urea (6 mL, 10 mM) was added into the mixture with continuously stirring for 30 min. After the mixture was heat-treated at 140 °C for 10 hrs inside a 25 mL Teflon-lined stainless-steel autoclave, the precursor of CuNiFe-MMOs was obtained. This precursor and 10 mg of $NaHCO_3$ were then mixed with 15 mL ethylene glycol, followed by a solvothermal reduction process performed at 160 °C for 2 hrs. After the reaction solution was naturally cooled down to room temperature, the re-CuNiFe-MMOs were collected by washing alternatively using water and ethanol for three times and then dried under vacuum at 60 °C for 2 hrs. Preparation methods of re-CuFe-MMOs, re-CuNi-MMOs, and re-FeNi-MMOs were similar to those of re-CuNiFe-MMOs, except that the elements of Ni, Fe and Cu were not available in the raw materials, respectively.

2.2. Characterization methods

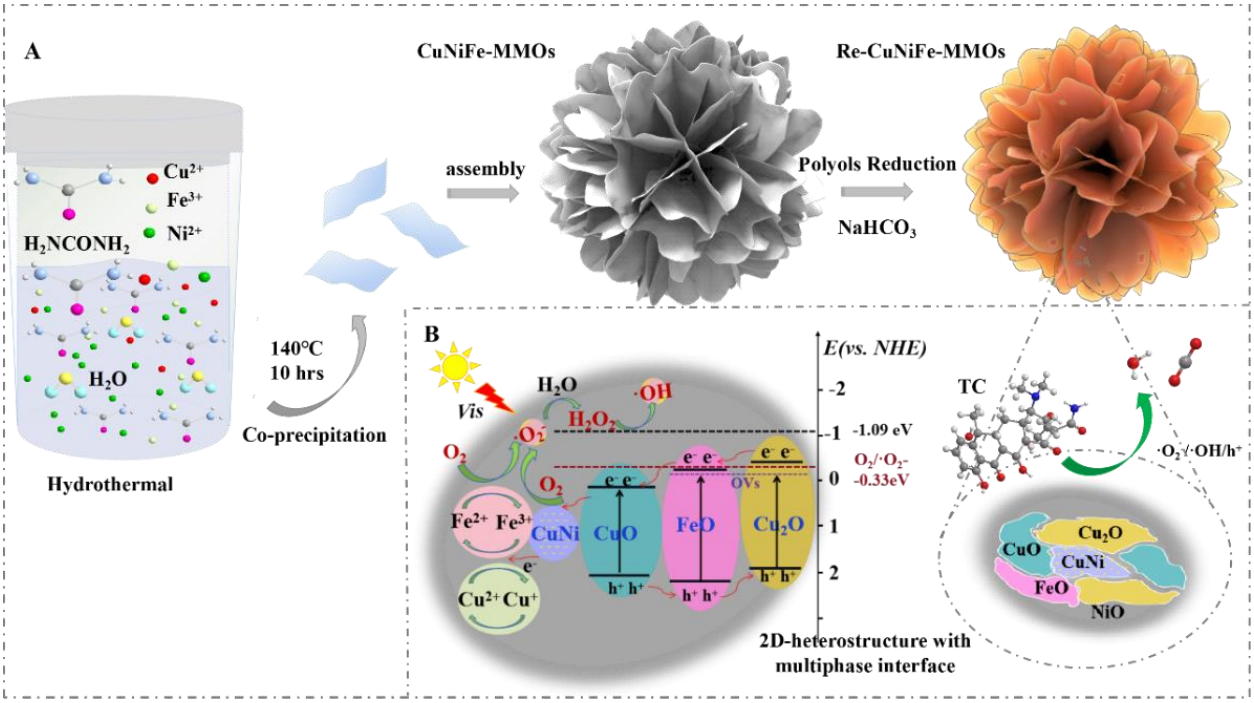

Fig. 1. Schematic illustration for (A) the fabrication of re-CuNiFe-MMOs 2D-heterostructure and (B) Its Fenton-like photocatalytic mechanism for TC degradation.

Microstructures and morphology of the samples were characterized using a field emission scanning electron microscope (FE-SEM, JEOL, S-4800), a transmission electron microscope (TEM, JEOL JEM-2100) with a selective region electron diffraction (SAED) function. Element distribution inside the samples was detected using an energy-dispersive X-ray spectrometer (EDS, TN5400, 15 keV). Crystalline structures of the samples were measured using a powder X-ray diffraction (XRD, Bruker D8, with Cu Kα as the source of radiation). Surface area of the prepared materials was measured using a Brunauer-Emmett-Teller (BET, Micromeritics TRISTAR 3020 V) method. Surface functional groups were analyzed using a Fourier transform infrared spectroscope (FT-IR, Nicolet IS10). Molecular structures were studied using a Raman spectroscope (InVia microconfocal spectrometer, Renishaw Corporation) with He-Ne laser at a wavelength λ of 514 nm and a power of 10~20 mW. The element bonding information and the valence band positions (E_{VB}) were studied using an X-ray photoelectron spectroscope (XPS, PHI-5000C ESCA system) with Al Kα as the radiation source, and calibrated using C 1s of surface contaminant at 284.6 eV. UV-vis diffuse reflectance spectroscopy (Cary 5000 UV-Vis-NIR with a Pb smart detector) was used to monitor the bandgaps of materials under the wavelength range of 200-800 nm. The efficiency of photogenerated charge transfer was tested using a photoluminescence spectroscope (PL, F-7000, Hitachi Limited). Analysis using electrochemical impedance spectroscopy (EIS) was performed using an electrochemical Workstation (CHI660E, Shanghai Chenhua). Electron paramagnetic resonance (EPR) spectra (Miniscope MS-5000 EPR spectrometer at 293 K) were conducted with 5,5-Dimethyl-1-pyrroline N-oxide (DMPO) and 2,2,6,6-tetramethylpiperidine (TEMP) used as spin probes.

2.3. Assessment of Fenton-like photocatalytic performance

Fenton-like photocatalytic activities of the prepared catalysts against TCs (including tetracycline (TC), chlortetracycline (CTC), oxytetracycline (OTC)), non-tetracycline antibiotics of ampicillin (AMP) and kalamycin (KAN) were tested in a multi-tube photo-catalytic reaction equipment (JOYN-GHX-BC, Shanghai Joyn Electronic CO., Ltd.) with a 150 W Xe lamp, which was equipped with a cut-off filter (λ>420 nm) to obtain a visible light source. In experiments, 10 mg of the catalyst was firstly mixed into an antibiotic solution (40 mL, 10 mg·L^{-1}), and kept in dark under N_2 for 30 min to achieve an adsorption-desorption equilibrium before the visible-light irradiation. During the degradation of TCs, 3 mL of suspension was removed at a regular period with a 0.22 μm wavelength filter. The concentration of TCs was determined based on its absorbance wavelength using a UV-vis spectrophotometer (UV-1800, Shimadzu). The intermediates generated during the degradation process were analyzed using a liquid chromatography-mass spectrometry (LC-MS, Varian 310). The mineralization efficiency was quantified using a total organic carbon (TOC) analyzer (TOC-VCPH, Shimadzu). For identifying the contribution of ROSs, radical trapping tests were performed by adding scavengers into a mixed solution of antibiotics, including triethanolamine (TEA, 1 mM), benzoquinone (BQ, 0.01 mM), isopropanol (IPA, 1 mM), and furfuryl alcohol (FFA, 1 mM). To detect superoxide radicals ($\cdot O_2^-$) and hydroxyl radicals (·OH), 10 mg of sample powder and 10 μL DMPO were evenly dispersed in 2 mL deionized water, then the suspensions were illuminated under a 150 W Xe lamp with a UV cutoff filter (λ>420 nm) for 4 min and the supernatants of the suspension were collected for analysis using EPR spectroscopy. Meanwhile, using the same detection method as described above, TEMP was used as a spin trap to detect singlet oxygen ($^1O_2$). For evaluating the degradation of TC into CO_2, H_2O, and other inorganic small molecules, 50 mg·L^{-1} of TC was subjected to Fenton-like photocatalytic degradation, and 20 mL of the suspension was taken out at a regular period with a 0.22 μm filter. Finally, *E. Coli* culture experiments were performed in the above taken-out solution for verifications (Text S2).

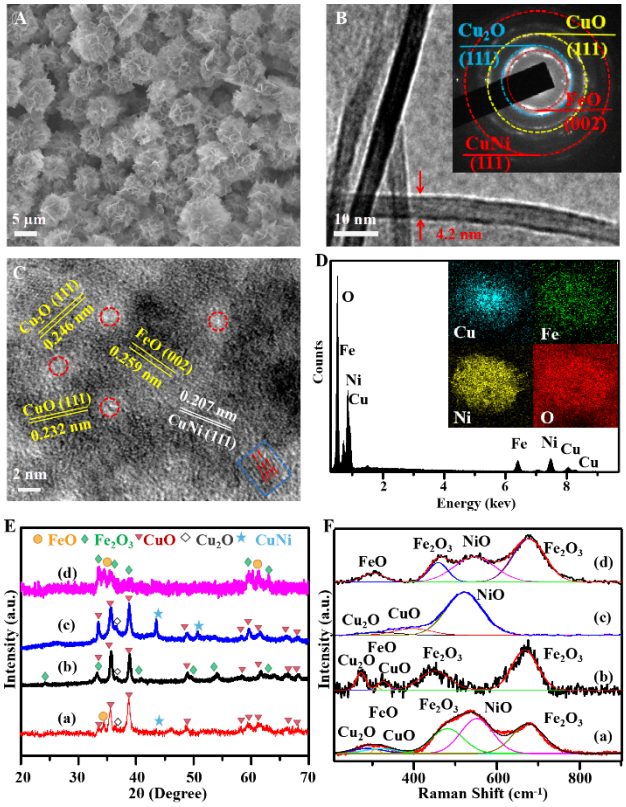

Fig. 2. (A) SEM image, (B) TEM image with inset SADE pattern, (C) HRTEM image, (D) EDS pattern with inset elemental mapping of re-CuNiFe-MMOs catalyst. (E) XRD patterns and (F) Raman spectra for re-CuNiFe-MMOs (a), re-CuFe-MMOs (b), re-CuNi-MMOs (c), and re-FeNi-MMOs (d).

3. Results and discussion

3.1 Synthesis and characterization

Fenton-like photocatalyst of the cluster structure assembled by re-CuNiFe-MMOs hetero-nanosheets has been synthesized through the HPSR process, as illustrated in Fig. 1A. At beginning, the urea is gradually hydrolyzed into ammonia and carbonate at 140 °C, which creates an alkaline condition, thus offers plentiful nucleation sites and CuNiFe-MMOs nanosheets are formed within the confined growth space. Then, three-dimensional (3D) assembly of these nanosheets gradually results in the orientation arrangement of nanosheets, which are perpendicular each other to lower their interaction energy (Fig. S1).[22] Subsequently, the reduction of CuNiFe-MMOs at 160 °C ethylene glycol in the solvothermal system

with assistance of $NaHCO_3$ has produced multimetal and multivalent re-CuNiFe-MMOs with multiphase interfaces. Fig. 2A and 2B present that the re-CuNiFe-MMOs show nanosheet-assembled clusters with an average nanosheet (7 layers) thickness of 4.2 nm and an average specific surface area of 126 $m^2 \cdot g^{-1}$ (Fig. S2, Table S1). Such stable cluster structure can offer the amount of exposed active sites and maximize their catalytic activities. Its SAED pattern exhibits the polycrystalline nature (Fig. 2B inset), in which different diffraction rings are identified as the facets of FeO (002), Cu_2O (111), CuO (111), and CuNi (111), respectively. HRTEM measurement image shows their corresponding lattice spacings of 0.259, 0.246, 0.232, and 0.208 nm (Fig. 2C). Meanwhile, the disordered regions (marked in red circles) and the dislocations of lattice fringes (marked in a blue circle) on the surfaces of re-CuNiFe-MMOs nanosheets are corresponding to the amorphous structures or structural defects (e.g. OVs and grain boundaries).[24] Moreover, EDS results prove the existence of Cu, Fe, Ni and O elements which have uniformly distributed on re-CuNiFe-MMOs nanosheets (Fig. 2D). In Fig. 2E, the XRD peaks of re-CuNiFe-MMOs at 35.5°, 38.7°, 48.7°, 61.5°, 66.2°, and 68.1° are attributed to the $(11\bar{1})$, (111), $(20\bar{2})$, $(11\bar{3})$, $(31\bar{1})$, and (220) faces of CuO, respectively (JCPDS No. 48-1548). The peak of CuNi alloy (JCPDS No. 09-0205) at 43.5° is located between those of Cu (JCPDS No. 04-0836) and Ni (JCPDS No. 65-0380). The Cu_2O at 36.5° (JCPDS No. 65-3288) and FeO at 34.5° (JCPDS No. 49-1447) also co-exist, while NiO remains amorphous without showing any diffraction peaks. XRD peaks of Cu oxides, Fe oxides and CuNi-alloy have not been detected in the samples of re-FeNi-MMOs, re-CuNi-MMOs, and re-CuFe-MMOs, respectively. The exist of multiphases also can be confirmed by Raman spectra (Fig. 2F). The peaks of 303, 320 and 553 cm^{-1} which are assigned to the Fe-O, Cu-O, and Ni-O stretching vibration mode of FeO, CuO, and NiO, respectively.[25-27] The peak of 286 cm^{-1} is the symmetrical stretching of Cu-O for Cu_2O. The peaks at 480 and 675 cm^{-1} are due to Fe-O vibration for the inevitable Fe_2O_3 in air.[28] All the above peaks can be observed in re-CuNiFe-MMOs, whereas the peaks of Ni-O, Fe-O, and Cu-O are absent in re-CuFe-MMOs, re-CuNi-MMOs, and re-FeNi-MMOs, respectively. For all the samples, the positions of Fe-O and Ni-O peaks remain nearly unchanged, whereas the re-CuNiFe-MMOs shows that the Cu-O peaks are red-shifted compared with those of re-CuFe-MMOs, but are blue-shifted compared to those of re-CuNi-MMOs.[29]

3.2 Fenton-like photocatalytic performance

The catalytic performance of re-CuNiFe-MMOs was evaluated by UV-vis spectra for TCs degradation under visible light irradiation. The ring-opening degradation of TC molecules can be identified by two characteristic absorption peaks at 370 nm (benzene) and 245 nm (naphthalene) (Fig. S3).[30] In this Fenton-like photocatalysis reaction system, the synergistic effect of FeO and the multivalent oxidation states of Cu significantly enhances the capability for TC degradation even without adding H_2O_2. Fig. 3A shows that with an initial TC concentration of 10 $mg \cdot L^{-1}$ at a pH value of 7.2 and a catalyst dosage of 0.25 $g \cdot L^{-1}$, TC is hardly degraded without using any catalyst under the visible light irradiation. Whereas using the optimized re-CuNiFe-MMOs without H_2O_2 (Fig. S4-S6), an optimal TC removal rate of 99.9% can be achieved in 4 mins with a constant reaction rate (K) of 1.65min^{-1}, which is extremely higher than 72.1% (K=0.44 min^{-1}) of re-CuFe-MMOs (Figs. S7A and Fig. S8A), 60.6% (K=0.23 min^{-1}) of re-CuNi-MMOs (Figs. S7B and Fig. S8B) and 46.5% (K=0.12 min^{-1}) of re-FeNi-MMOs (Figs. S7C and Fig. S8C). The good linear relationship between ln (C_t/C_0) and the irradiation time reveals its the pseudo-first-order kinetics (Figs. S8D). Besides, the re-CuNiFe-MMOs shows a much better catalytic performance than CuNiFe-MMOs (Fig. S9), confirming that the Fenton-like photocatalytic activity is mainly derived from FeO and the multivalent oxidation states of Cu. Owing to the existence of amphoteric molecules, pH variation will result in different molecule forms of TC. TC exists as a protonated TC^+ when pH< 4, whereas it is mainly in the form of neutral TC at pH of 4-7.5. It becomes the anion TC^- when pH>7.5. Clearly, the pH value influences the adsorption capacity and performance of the catalyst. In our case, under the visible light irradiation for 4 min by using re-CuNiFe-MMOs catalyst, the TC's removal rates is increased from 28.1% to 78.2% with the pH value increased from 3.0 to 4.5. It can reach nearly 100% at pH of 7.2, whereas it is gradually decreased from 62.2% to 51.6% with the pH value further increased from 9.5 to 11.0 (Fig. 3B and Fig. S10). This can be explained by the fact that the electron density of TC in its neutral condition is much higher than those in the acidic or alkaline condition, which is conducive to the attack of free radical species.[31] Meanwhile, the $\cdot O_2^-$ is the dominant free radical in the neutral pH value, which maintains a high degradation efficiency of TC.[32] Whereas at the acidic or basic conditions, a large amount of H^+ or OH^- will react with $\cdot O_2^-$ or the catalyst to a certain extent, which directly affects the degradation performance of the catalyst on TC.[33] As discussed above, the polyol reduction results in the multiphases and associated rich OVs on catalyst surface, thus suppressing the recombination of photogenerated electrons and holes, together with the assistance of Fenton-like effect, thereby improving the visible light-induced Fenton-like photocatalytic degradation performance.

As contrast, in Fig. 3C, H_2-reduced CuNiFe-MMOs (Fig. S11) is largely inferior in performance at the same conditions for polyol-reduced re-CuNiFe-MMOs. This is mainly due to the surface -OH groups can produce a large number of H_2O_2 which is involved in Fenton-like reaction system of re-CuNiFe-MMOs. It can be proven by the catalase tests in the TC degradation process. The catalase can consume the produced H_2O_2 during the reaction with 76.8% degradation by using polyol-reduced re-CuNiFe-MMOs catalyst, but the degradation rate hardly changed when using H_2-reduced re-CuNiFe-MMOs catalyst. It also proves that the H_2O_2 produced by the surface -OH groups in the catalytic reaction system of re-CuNiFe-MMOs avoids the utilization of the additional oxidants in our Fenton-like reaction. Further investigations of recyclability and stability were performed for the re-CuNiFe-MMOs catalyst toward TC degradation. The Fenton-like photocatalytic degradation efficiency can be maintained at 95.5% over 12 cycles without showing apparent morphology changes (Figs. S12, S13, and S14, Table S2). The slightly decrease of degradation performance is mainly due to the attachment of degraded intermediates on the catalyst's surface. As a contrast, the degradation rates of re-CuFe-MMOs, re-CuNi-MMOs, and re-FeNi-MMOs are significantly reduced to 22.2%, 13.4%, and 11.6% after 12 cycles, respectively, which are all much smaller than that of re-CuNiFe-MMOs (Fig. 3D). For demonstration of applications, the re-CuNiFe-MMOs was

further applied to catalyze the high concentrations TC degradation. At TC's concentrations of 10, 25, 50, 75, and 100 mg·L^{-1}, the obtained degradation rates are 99.9%, 94.6%, 90.8%, 87.4%, and 82.7% with a K value of 1.65, 0.075, 0.040, 0.023, and 0.015 min^{-1}, respectively, under a visible light irradiation for 120 min (Fig. 3E). Since the degradation of high concentrations TC produces a large number of intermediates, which competes with its parent molecules for occupying the active sites on catalyst's surface, thus inhibiting its photocatalytic degradation efficiency. Additionally, TC degradation can also be confirmed via its mineralization efficiency which is quantified by the TOC value (Fig. 3F). Catalyzed by re-CuNiFe-MMOs, the decomposition efficiency of TC (50 mg L^{-1}) reaches 51.1% under the visible light irradiation for 15 min (Fig. S15), the TOC value becomes 26.4% at this moment. When the TC degradation rate reaches 98.2% after 90 min, the TOC value becomes 70.2%, indicating most of the TC is degraded to CO_2 and H_2O, and only a few are degraded into organic small molecule intermediates, which would be further degraded into harmless inorganic matters as the reaction continued. The above two values are much higher than 74.4% (K=0.0077 min^{-1}) and 44.8% for the re-CuFe-MMOs, 62.1% (K=0.0038 min^{-1}) and 40.5% for re-CuNi-MMOs, 51.3% (K=0.0035 min^{-1}) and 37.7% for re-FeNi-MMOs, respectively. Thus, the synergistic effect of photocatalysis and Fenton-like process could greatly promote the TC degradation in a high concentration. This synergetic effect can also be demonstrated by testing the proliferation concentration of *E. coli.* As shown in Fig. 3G, the living *E. coli* has a concentration of 17,500 cfu mL^{-1} in the original 50mg L^{-1} TC solution, whereas the number of *E. coli* within the TC solution degraded catalyzed by re-CuNiFe-MMOs is increased to ~52,000,000 cfu mL^{-1} after proliferation in 37 °C for 12 hrs, indicating TC concentration is degraded to less than 1 mg L^{-1}.

In addition, the universality of re-CuNiFe-MMOs was further investigated toward the catalytic degradation of chlortetracycline (CTC) and oxytetracycline (OTC). As expected, the re-CuNiFe-MMOs exhibits outstanding catalytic activities for oxidation of both CTC and OTC (10 mg·L^{-1}), and the removal rates are 97.7% (K=0.57 min^{-1}) and 93.3% (0.32 min^{-1}) in 10 min, respectively (Fig. 3H, Fig. S16). All the above analysis results indicate that re-CuNiFe-MMOs with multiple-nanophases and stable 2D hetero-nanostructured clusters allow the excellent Fenton-like photocatalytic performance and

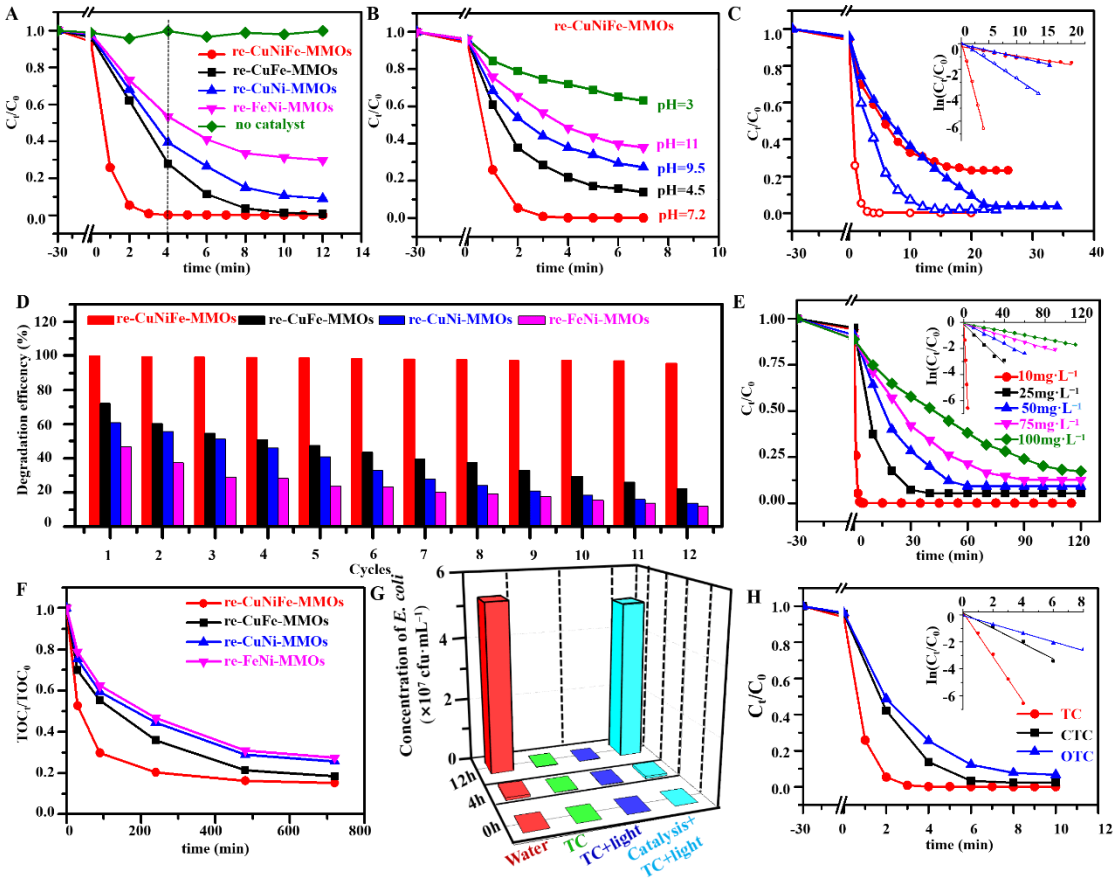

Fig. 3. (A) Profiles of TC degradation catalyzed by the prepared catalysts and (B) of different pH over re-CuNiFe-MMOs. (C) Profiles of TC degradation with inset corresponding pseudo-first-order kinetic models over polyols reduced CuNiFe-MMOs (red) and H_2 reduction CuNiFe-MMOs (blue) with catalase (solid) and without catalase (hollow). (D) The histogram of corresponding degradation efficiency for cycling test catalyzed by the prepared catalysts. (E) The degradation for high concentration of TC using re-CuNiFe-MMOs catalyst. (F) The TOC removal efficiency using the prepared catalysts. (G)Histogram with the reproduction concentration of *E. coli* in solution culture after TC degradation in different time. (H) The degradation rate of TCs catalyzed by re-CuNiFe-MMOs. (Operating parameters: after 30 min adsorption equilibrium under anaerobic dark conditions, 0.25 g L^{-1} catalyst, 10 mg L^{-1} TC (A-D, H), 50 mg L^{-1} TC (F, G), 25 °C, pH 7.2).

reusability toward TC degradation, which creates great prospects for their practical applications. Besides, two kinds of non-tetracycline antibiotics, AMP and KAN are selected to verify the universality for degradation performance (Table S3 and Fig. S17). The degradation rates of AMP and KAN in 10 mg·L^{-1} under visible light are 97.8% (16 min, K=0.25 min^{-1}) and 97.0% (20 min, K=0.18 min^{-1}), respectively, further confirmed re-CuNiFe-MMOs is universal applicable to the degradation of other types of antibiotics.

3.3 Intermediates and pathway of TC degradation

Based on above analysis, the re-CuNiFe-MMOs system enables the Fenton-like photocatalysis process to produce numerous $\cdot O_2^-$, causing the generation of a series of intermediates during the degradation of TC, which can be monitored by LC-MS. The MS's full scan mode was used to select the mass-to-charge ratio (m/z) values of the main intermediates, the obtained results are shown in Fig. S18. The possible molecular structures of the main intermediates are listed in Table S3. Functional groups (e.g., amine groups, phenolic groups, and double bond) of TC can be attacked by $\cdot O_2^-$and ·OH due to their relatively high electron densities. Different types of intermediates (26 in total) can be monitored during the Fenton-like photocatalysis process for TC's degradation. Loss of functional groups and ring opening reactions are the two main decomposition mechanisms of TC for the phenomena of dehydroxylation, demethylation, hydroxylation, and amide bond cleavage.[16]

According to the above results, three possible TC degradation pathways were proposed, as shown in Fig. 4. For route I, the C14 and C15 double bonds with their highest electron density in TC are preferentially attacked by ROSs to generate primary intermediates of TC1 (m/z=461). Reactions with ROSs at the C1 and C18 double bonds of TC1 can produce an intermediate of TC4 (m/z=477). TC4 undergoes a dehydroxylation reaction at position C6 to form TC8 (m/z=459), followed by a deamidation reaction at position C18 to generate TC12 (m/z=400). TC15 (m/z=343) is also produced after the removal of the amino and methyl groups of TC12 at the positions C2 and C6, respectively. For route II, the TC molecule is converted to produce TC2 (m/z=431) because of the demethylation process at position C2. Thereafter, the demethylation at positions C2 and C6 and dehydroxylation reaction at position C13 of TC2 produce TC5 (m/z=403). Subsequently, TC5 can undergo a series of processes of deamination, dehydrogenation, and amide bond cleavage, at positions C2, C14 and C15, C18, respectively, resulting in the formation of TC9 (m/z=376). Thereafter, TC9 undergoes dehydrogenation at positions C3 and C4, and is further degraded by the oxidatives, undergoing loop opening and hydroxylation at C7 and C12 to generate TC16 (m/z=337). After that, due to the unstable structure of the enol type in TC16, it will be transformed into a ketone type,[34] and a ring-opening reaction would occur to produce TC18 (m/z=297).[16] Simultaneously, the dehydroxylation reaction of TC2 occurs at position C6 to form TC6 (m/z=417). The ·OH radical can attack positions C1, C2, C13 and C18, TC7 to form TC10 (m/z=352) through dehydroxylation and deamination reaction. Then, due to the attack of ·OH radicals, the deamination reactions at position C2 and the cleavage of C1 and C18 double bonds of TC10 generate TC13 (m/z=318). Further dehydroxylation and demethylation reactions at position C2 and C6 of TC13 produce TC17 (m/z=301). This TC17 undergoes different reactions of demethylation, hydroxylation, ketoneization, double bond cleavage, ring-opening reaction, dialdehyde reaction at positions C3, C4, C6, C8, C11, and C16 respectively to form TC18 (m/z=297). For route III, hydrogen and hydroxyl at positions C5 and C6 on TC are dehydrated and converted into anhydrous tetracycline TC3 (m/z=427). Through TC3 demethylation in the amino group at position C2, TC7 (m/z=399) appears. The amide at position C18 of TC6 is attacked by free radicals, which is further deaminated and converted into TC11 (m/z=384). Afterward, TC11 undergoes a ring-opening reaction at position of C18, resulting in the formation of TC14 (m/z=346). As the degradation reaction is further progressed, these intermediates are further oxidized into organic small molecules with their m/z values of 274, 256, 230, 200, 189, 183, 148 and 84 through a series of dissociation and ring-opening processes. Finally, above products are mineralized into harmless inorganic substances by the generated ROSs in the reaction system, and the TC structure is completely destroyed.

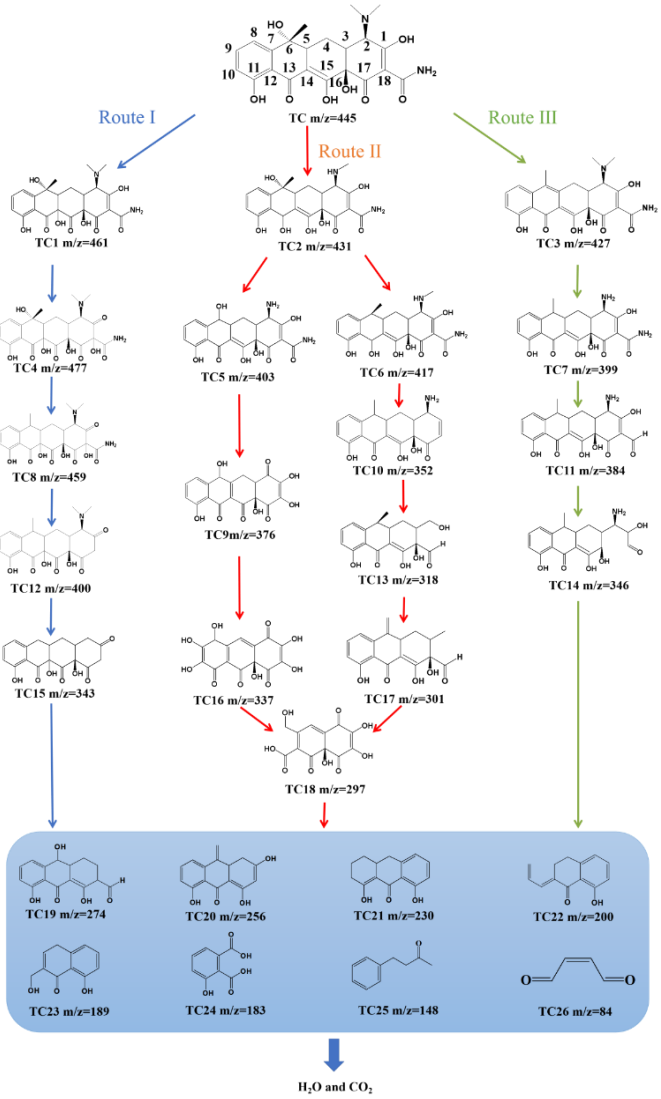

Fig. 4. The pathways for TC degradation in the re-CuNiFe-MMOs system under visible light irradiation.

3.4. Catalytic reaction mechanism

The further understanding is carried out to reveal the catalytic mechanisms for TC degradation. At first, XPS spectra were more compared for the fresh and used re-CuNiFe-MMOs (Fig. 5). As expected, the elements of Cu, Fe, Ni, O can be clearly detected from the survey spectra (Fig. S19). The high-resolution spectrum of Cu 2*p* has two strong peaks at 933.1 and 952.9 eV for the spin orbits of Cu 2*p* 1/2 and Cu 2*p* 3/2, which can be decomposed into three pairs of peaks, i.e., 932.1 and 952.1 eV, 933.0 and 952.8 eV, 933.7 and 953.7 eV, corresponding to Cu^0, Cu^+ and Cu^{2+}, respectively (Fig. 5A).[35] After applied to degrade TC, in the fresh and used re-CuNiFe-MMOs, the percentage of Cu^{2+} was decreased significantly from 69.5% to 58.7%, whereas the percentages of Cu^+ and Cu^0 are increased from 21.4% to 27.5%, and 9.1% to 13.8%, respectively. In Ni 2*p*, the peaks of Ni 2*p*3/2 and Ni 2*p*1/2 can be divided into two pairs of peaks, i.e., 855.0 and 872.8 eV, 856.0 and 873.7 eV (Fig. 5B). They can be assigned to Ni^0 and Ni^{2+}, respectively, corresponding to those of CuNi and NiO. Before and after used in catalytic reaction, the percentage of Ni^0 is decreased from 30.1% to 26.6%, meanwhile the percentage of Ni^{2+} is increased from 69.9% to 73.4%. For Fe 2*p*, two strong peaks of 712.1 (Fe 2*p* 3/2) and 723.8 eV (Fe 2*p* 1/2) can be divided into two pairs of peaks at 710.7 and 723.2eV, 713.7 and 726.2 eV, corresponding to Fe^{2+} and Fe^{3+}, respectively (Fig. 5C).[16] The percentage of Fe^{2+} for the used one is increased significantly from 49.3% to 57.2%, accompanying with the decrease of Fe^{3+} contents from 50.7% to 42.8%. In brief, XPS analysis shows that during the Fenton-like photocatalytic degradation of TC by the re-CuNiFe-MMOs, an increased proportion of high-valence Cu2+ and Fe3+ is partially converted to Cu^+ and Fe^{2+}, which demonstrates that changes in Fe(II)−Fe(III) and Cu(I)−Cu(II) occur during the radical generation.[2] Besides, there are three deconvoluted O 1*s* peaks at 530.6, 531.2 and 531.8 eV corresponding to lattice oxygen, defect oxygen and hydroxyl oxygen, respectively (Fig. 5D).[36] The degradation reaction causes that the proportions of lattice and defect oxygen are decreased from 39.8% to 32.0% and 34.2% to 33.1%, respectively, due to their activation for the dissolved oxygen[37], while those of hydroxyl oxygen is increased from 26.0% to 34.9% because of the attachment of constantly generated OH^- on the surface of re-CuNiFe-MMOs.

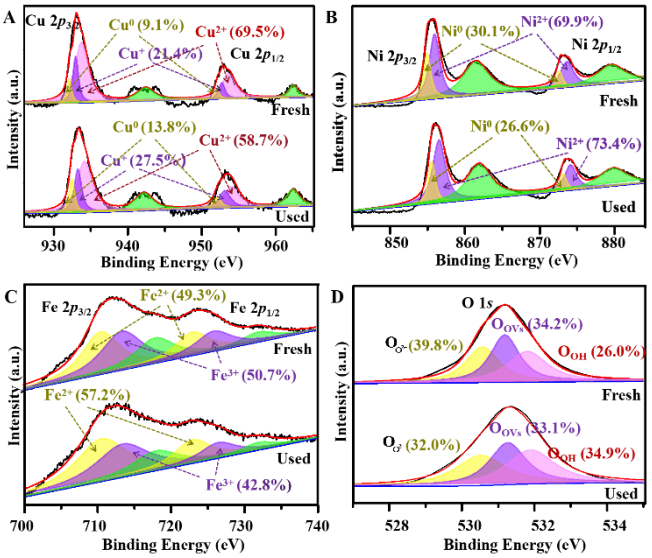

Fig. 5. The detailed XPS spectra analysis for the fresh and used re-CuNiFe-MMOs catalyst.

Then, optical absorption properties of the samples were analyzed by UV–vis DRS. In Fig. 6A, owing to multiple valence of Cu, the re-CuNiFe-MMOs, re-CuFe-MMOs, and re-CuNi-MMOs all exhibit strong light absorption capabilities, which are mainly due to the excitation transition of Cu 3d^9 from $d_{x^2-y^2}$ to d_{xy}. Meanwhile, iron oxides contained samples of re-CuNiFe-MMOs, re-CuFe-MMOs, and re-FeNi-MMOs show the red shifts. According to the relationship of tangent of $(\alpha h\upsilon)^2$ and energy ($h\upsilon$),[38] the corresponding bandgap energies (Eg) of re-CuNiFe-MMOs, re-CuFe-MMOs, re-CuNi-MMOs and re-FeNi-MMOs were calculated and their obtained results are

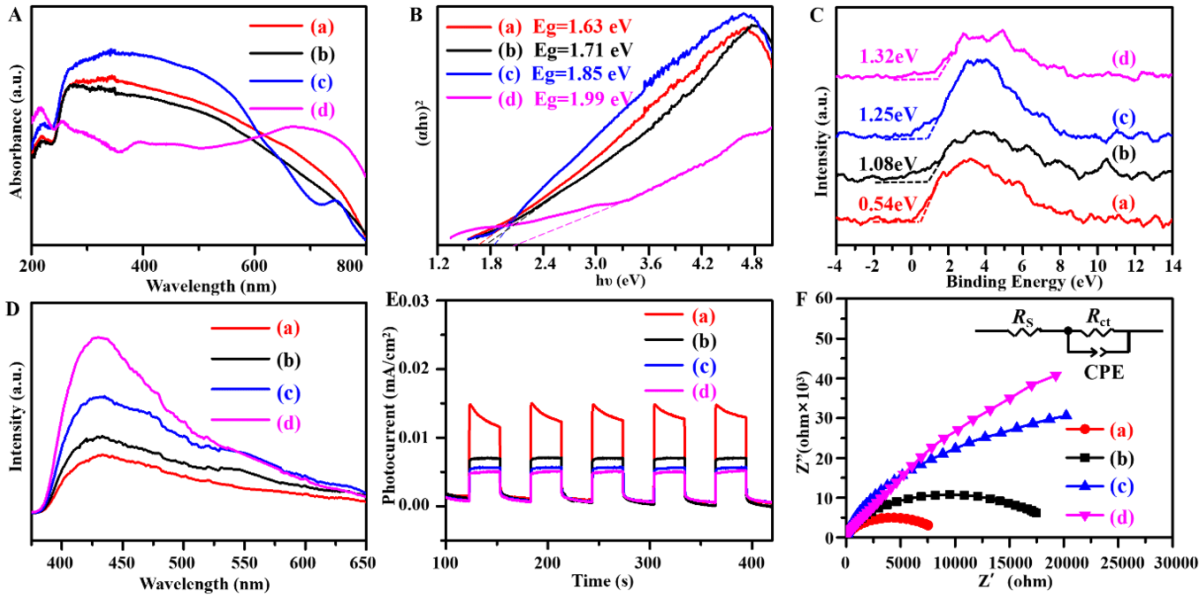

Fig. 6. (A) UV–vis DRS spectra, (B) Tauc's plots, (C) VB-XPS spectra, (D) PL spectra, (E) Transient photocurrent curves, (F) Nyquist plots of EIS for the prepared samples. ((a) re-CuNiFe-MMOs, (b) re-CuFe-MMOs, (c) re-CuNi-MMOs, (d) re-FeNi-MMOs).

1.63, 1.71, 1.85 and 1.99 eV, respectively (Fig. 6B). These data agree well with the calculated ones using the formula of Eg (eV) = 1240·λ^{-1} (where λ is the wavelength of maximum absorption). Since the band structure determines generation and migration of the photogenerated carriers, the valence band positions (E_{VB}) were studied by using VB-XPS (Fig. 6C). The E_{VB} values of re-CuNiFe-MMOs, re-CuFe-MMOs, re-CuNi-MMOs, and re-FeNi-MMOs are 0.54, 1.08, 1.25, and 1.32 eV, respectively. Their corresponding conduction band edge potentials (E_{CB}) are calculated to be -1.09, -0.63, -0.60 and -0.67 eV, respectively, according to the Eq. $E_{CB}=E_{VB}-E_g$. Because the E_{CB} value is more negative than the potential of $O_2/{\cdot}O_2^-$ (-0.33 eV vs. NHE), the dissolved O_2 in the solution can be converted to ${\cdot}O_2^-$ by the activation of conduction band electrons. Hence, the re-CuNiFe-MMOs has the highest negative value of E_{CB}, which is the most efficient one to produce ${\cdot}O_2^-$ for high catalytic activity.

Separation capabilities of photogenerated e^-/h^+ pairs were further investigated by employing PL, photocurrent, and EIS analysis. PL intensity is significantly influenced the photocatalytic activity, since its emission signal is derived from the energy released by the recombination of carriers.[16] Fig. 6D presents the emission spectra of the prepared samples under an excitation wavelength of 350 nm. A strong emission peak at 430 nm can be observed and the emission peak intensity order for the prepared catalysts is re-FeNi-MMOs > re-CuNi-MMOs > re-CuFe-MMOs > re-CuNiFe-MMOs. The smallest emission peak intensity of the re-CuNiFe-MMOs clearly indicates its best separation efficiency for the photoexcited carriers. The separation efficiency of photogenerated e^-/h^+ pairs can be revealed by transient photocurrent responses and impedance technique. Generally, the stronger the photocurrent responses is, or the smaller the impedance is, the more effective that the photogenerated electrons and holes can be separated, which leads to the higher photocatalytic activity. Fig. 6E clearly illustrates that the re-CuNiFe-MMOs has the highest photocurrent density. Meanwhile, EIS Nyquist curve of re-CuNiFe-MMOs in Fig. 6F plots a minimum impedance to transfer electrons, and the corresponding equivalent circuit diagram is given in the inset of Fig. 6F.

What's more, the radical trapping experiments were carried out to prove the active species produced during the oxidative degradation on photocatalyst surface.[39] Herein, triethanolamine (TEA), tert-butanol (TBA), p-benzoquinone (BQ) and furfuryl alcohol (FFA) were selected as the probe reagents to quench h^+, ·OH, ${\cdot}O_2^-$and $^1O_2$ radicals, respectively. As depicted in Fig. 7A and Fig. S20A, the additions of TBA, FFA, TEA and BQ decrease the degradation rates of TCs from 99.9% to 87.4%, 42.0%, 23.6% and 8.1%, respectively, whereas almost all TC can be degraded if scavenger was absent. It indicates that ${\cdot}O_2^-$ radicals has contributed to the photocatalytic reaction, which can be confirmed by the scavenge experiments under an anaerobic condition (Fig. S20B). Compared with that of only 6.7% without any scavenger, the TC degradation is only 3.4%, 4.5%, 6.0% and 5.3%, which are almost unchanged after trapping ${\cdot}O_2^-$, h^+, ·OH and $^1O_2$ with BQ, TBA, TEA and FFA. Contrast with the results of re-CuFe-MMOs, re-CuNi-MMOs, and re-FeNi-MMOs, the re-CuNiFe-MMOs shows the highest catalytic degradation efficiency and is strongly affected by the trapping reagents, due to the generated numerous active species. The radical trapping experiments for CTC and OTC clearly show that ${\cdot}O_2^-$plays a key role in the photocatalytic degradation reaction of TCs in the re-CuNiFe-MMOs catalysis system. In addition, the capture experiment has also been carried out at aerobic or anaerobic conditions in the dark (Fig. S21). The results confirmed that the main active oxygen species to degrade TC is ${\cdot}O_2^-$ under dark conditions.

To further gain the insight into the effects of defects (e.g., OVs) on the catalyst, the EPR tests were performed (Fig. 7B and Fig. S22). The EPR line widths of the prepared samples are broadened due to

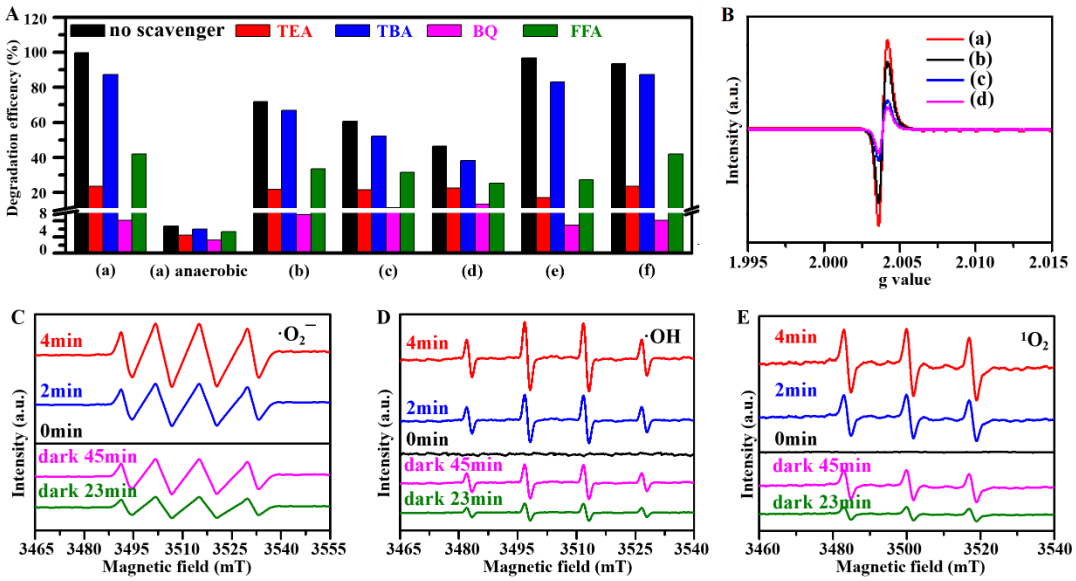

Fig. 7. (A) The effect of radical scavengers on degradation of TC by the prepared catalysts at aerobic or anaerobic conditions under visible light irradiation, respectively. (B) EPR patterns of the prepared catalysts. (C-E) EPR spectra of ${\cdot}O_2^-$, ·OH, and $^1O_2$ by using re-CuNiFe-MMOs under visible light and dark in different reaction time, respectively. ((a) re-CuNiFe-MMOs, (b) re-CuFe-MMOs, (c) re-CuNi-MMOs, (d) re-FeNi-MMOs, (e) CTC, (f) OTC). (Operating parameters: 0.25 g L^{-1} catalyst, 25 °C, 10 mg L^{-1} TC, pH 7.2).

the generated copper oxide (Cu-O) or ferrite oxide (Fe-O) vacancies. Both the re-CuNiFe-MMOs and re-CuFe-MMOs show relatively higher and broader signal intensities with g ($h\gamma/\mu_B B$) of 2.0025 - 2.0060 than re-CuNi-MMOs and re-FeNi-MMOs with g of 2.0035-2.0055, respectively. This is mainly due to the greater number of defects caused by the multiple oxidation states of Cu and Fe. The vacancy defects can promote charge separation and they can be transformed into reactive species, thus leading to the enhanced Fenton-like photocatalytic activity. The generation of active species is further proved by EPR using DMPO and TEMP as spin-trapping reagent (Fig. 7C-E).[40] The signal intensities of $\cdot O_2^-$, ·OH and $^1O_2$ are increased obviously with the reaction time prolonged from 0 to 4 min under the visible light. The similar trend can be also observed when the Fenton-like reactions were progressed from 0 to 45 min under the dark conditions, although the signals are dramatically weaker. Besides, these signals' intensity attenuation can be observed according to the order of re-CuNiFe-MMOs < re-CuFe-MMOs < re-CuNi-MMOs < re-FeNi-MMOs under the same irradiation time (Fig. S23), confirming that re-CuNiFe-MMOs can produce the largest number of active species in the reaction process, thus showing the best TC degradation performance.

3.5. Fenton-like photocatalytic enhancing mechanism

Based on above analysis, the Fenton-like photocatalytic enhancement mechanism can be proposed for the efficiently degraded TCs in re-CuNiFe-MMOs system under the visible light irradiation, which is illustrated in Fig. 1B. The photogenerated electrons e^- from the valence band (VB) easily migrate to the conduction band (CB) at a relatively lower potential, thus leaving a lot of holes in its VB (Eq. (1)). Then, those electrons e_{CB}^- are transferred by CuNi nanophases immediately, and are captured by O_2 on the surface of catalysts. They can form the main sources to provide $\cdot O_2^-$, which promotes the migration and reaction of photogenerated electrons, thus accelerating the separation of carriers (Eq. (2)). Since the negative potential of CB (-1.09 eV) of re-CuNiFe-MMOs is much lower than the standard reduction potential O_2 ($E^\vartheta(O_2/\cdot O_2^-)$ = -0.33 eV vs NHE,[41] the electron trapped in the CB can be rapidly reduced the dissolved oxygen to $\cdot O_2^-$, which then form H_2O_2 by reacting with e_{CB}^- and H_2O (Eq. (3)).[42] The ·OH generated by e_{CB}^- and H_2O_2 (Eq. (4)) then react with $\cdot O_2^-$ to produce $^1O_2$ (Eq. (5)). Besides, the VB holes with a potential of 0.54 eV is insufficient to oxidize surface-adsorbed H_2O & OH^- to generate ·OH (($E^\vartheta(H_2O/\cdot OH)$ = 2.38 eV vs. NHE, $E^\vartheta(OH^-/\cdot OH)$ = 1.99 eV vs. NHE).[43] Those separated holes would directly involve in the catalytic oxidation of TC. For the re-CuNiFe-MMOs, the interfacial electron transfer can be significantly improved due to the redox cycles of Fe^{3+}/Fe^{2+} and Cu^{2+}/Cu^+, and the regenerated Fe^{2+} and Cu^+ significantly enhance the TC's degradation. The standard reduction potential of Cu^{2+}/Cu^+ is 0.17 eV and that of Fe^{3+}/Fe^{2+} is 0.77 eV, so Cu^+ can reduce Fe^{3+} via thermodynamically favorable electron transfer (Eqs. (6)-(9)).

re-CuNiFe-MMOs + hν → $h_{VB}^+ + e_{CB}^-$ (1)

$O_2 + e_{CB}^- \rightarrow \cdot O_2^-$ (2)

$\cdot O_2^- + H_2O + e_{CB}^- \rightarrow H_2O_2$ (3)

$e_{CB}^- + H_2O_2 \rightarrow \cdot OH + OH^-$ (4)

$\cdot OH + \cdot O_2^- \rightarrow OH^- + {}^1O_2$ (5)

$\equiv Fe^{2+}/\equiv Cu^+ + H_2O_2 \rightarrow \equiv Fe^{3+}/\equiv Cu^{2+} + \cdot OH + OH^-$ (6)

$\equiv Fe^{3+} + e_{CB}^- \rightarrow \equiv Fe^{2+}$, E^ϑ =0.77 eV vs NHE (7)

$\equiv Cu^{2+} + e_{CB}^- \rightarrow \equiv Cu^+$, E^ϑ =0.17 eV vs NHE (8)

$\equiv Fe^{3+} + \equiv Cu^+ \rightarrow \equiv Cu^{2+} + \equiv Fe^{2+}$ (9)

The polyols act as reductant in the catalyst preparation process, which can afford abundant-OH attached on the surface of re-CuNiFe-MMOs. These have been verified by the IR results (Fig. S24). The -OH groups act as the electron donors for TCs degradation, and the corresponding mechanism of O_2 activation is shown in Eqs. (10)-(11). According to Eqs. (12)-(14), secondary reactive species generated by $\cdot O_2^-$ (e.g. ·OH and $^1O_2$) then participate in the oxidative degradation processes based on the following Eqs.

re-CuNiFe-MMOs-OH + $O_2 \rightarrow$ re-CuNiFe-MMOs-O + $\cdot O_2^- + H^+$ (10)

$\cdot O_2^- + \cdot O_2^- + 2H^+ \rightarrow H_2O_2 + {}^1O_2$ (11)

$\cdot O_2^- + 2H_2O \rightarrow {}^1O_2 + H_2O_2 + 2H^+$ (12)

$\cdot OH + H_2O_2 \rightarrow HO_2\cdot + H_2O$ (13)

$HO_2\cdot \rightarrow H^+ + \cdot O_2^-$ (14)

$[2\equiv Cu^+, OVs] + O_2 \rightarrow [\equiv Cu^{2+} + \equiv Cu^+] + \cdot O_2^-$ (15)

$[2\equiv Fe^{3+}, OVs] + O_2 \rightarrow [\equiv Fe^{3+} + \equiv Fe^{2+}] + \cdot O_2^-$ (16)

$\cdot O_2^-/{}^1O_2/\cdot OH/h^+ + TCs \rightarrow CO_2 + H_2O +$ Inorganic ions (17)

In the Fenton-like photocatalytic degradation process, the OVs formed by the *in situ* reduction of CuNiFe-MMOs can adsorb O_2 and produce $\cdot O_2^-$ (Eqs. (15, 16)). Ultimately, TC on the catalyst surface is efficiently decomposed into CO_2, H_2O and other inorganic small molecules by all the ROSs formed in the system (Eq. (17)). In brief, the large specific surface area, exposed active sites, tunable band gaps, the valence changing of Cu and Fe, and abundant defects (e.g. OVs) are the key factors that the re-CuNiFe-MMOs system has the excellent catalytic activity for TCs degradation.

4. Conclusions

A cluster-structure assembled by re-CuNiFe-MMOs nanosheets have been integrated into HPSR process for TC degradation. Attributed to the 2D structured multiple-nanophases of alloy and MMOs with multivalent Cu ions, a large specific surface areas and numerous exposed active sites have been created. These 2D heterostructured clusters provide efficient mass transfer. Their interfaces of multiple-nanophases form abundant defects (e.g. OVs) and produce active radicals ($\cdot O_2^-$, $^1O_2$, ·OH and h^+). Therefore, the as-obtained re-CuNiFe-MMOs efficiently degrade TCs through the Fenton-like photocatalysis without using any additional oxidants. This work provides a green way for highly efficient Fenton-like photocatalysis in TCs degradation.

Author Contributions

Lin Fu; Investigation, Writing-original draft, Dandan Wu; Investigation, Analysis, Writing-original draft, Ming Wen; Supervision, Conceptualization, Methodology, Validation, Writing-review & editing, Yuanzheng Zhu; Writing-review & editing, Qingsheng Wu; Writing- review & editing, Tao Zhou; Writing-review & editing, Yongqing Fu; Writing-review & editing.

Conflicts of interest

There are no conflicts to declare.

Acknowledgements

This work was financially supported by the Science and Technology Committee of Shanghai Municipality (No. 21160710300, 19DZ2271500), the National Natural Science Foundation (NSFC No. 22171212), Interdisciplinary Joint Research Project of Tongji University (No. 2022-4-ZD-03, 2022-4-YB-12), the Shanghai Sailing Program (21YF1446800) from China, and the International Exchange Grant (IEC/NSFC/201078) through the Royal Society UK and NSFC."

References

1 Z.L. Li, C.S. Guo, J.C. Lu, Z. Hu, M. Ge, Tetracycline degradation by persulfate activated with magnetic Cu/$CuFe_2O_4$ composite: Efficiency, stability, mechanism and degradation pathway, *J. Hazard. Mater.,* 2019, **373**, 85-96.

2 J. Yu, J. Kiwi, I. Zivkovic, H.M. Rønnow, T. Wang, S. Rtimi, Quantification of the local magnetized nanotube domains accelerating the photocatalytic removal of the emerging pollutant tetracycline, *Appl. Catal. B: Environ.,* 2019, **248**, 450-458.

3 F. B. Yin, H. M. Dong, W. Q. Zhang, Z. P. Zhu, B. Shang, Antibiotic degradation and microbial community structures during acidification and methanogenesis of swine manure containing chlortetracycline or oxytetracycline, *Bioresour. Technol.,* 2018, **250**, 247-255.

4 T. Kaeseberg, J. Zhang, S. Schubert, R. Oertel, P. Krebs, Abiotic, biotic and photolytic degradation affifinity of 14 antibiotics and one metabolite e batch experiments and a model framework, *Environ. Pollut.,* 2018, **241**, 339-350.

5 S. Han, P. Xiao, Catalytic degradation of tetracycline using peroxymonosulfate activated by cobalt and iron co-loaded pomelo peel biochar nanocomposite: Characterization, performance and reaction mechanism, *Sep. Purif. Technol.,* 2022, **287**, 120533.

6 C. Wang, R. Sun, R. Huang, H. Wang, Superior fenton-like degradation of tetracycline by iron loaded graphitic carbon derived from microplastics: Synthesis, catalytic performance, and mechanism, *Sep. Purif. Technol.,* 2021, **270**, 118773.

7 W. Ding, X. Huang, W. Zhang, F. Wu, J. Li, Sulfite activation by a low-leaching silica-supported copper catalyst for oxidation of As(III) in water at circumneutral pH, *Chem. Eng. J.,* 2019, **359**, 1518-1526.

8 Y. Gan, Y. Wei, J. Xiong, G. Cheng, Impact of post-processing modes of precursor on adsorption and photocatalytic capability of mesoporous TiO_2 nanocrystallite aggregates towards ciprofloxacin removal, *Chem. Eng. J.,* 2018, **349**, 1-16.

9 W.K. Jo, T. S. Natarajan, Facile Synthesis of Novel Redox-Mediator-free Direct Z-Scheme $CaIn_2S_4$ Marigold-Flower-like/TiO_2 Photocatalysts with Superior Photocatalytic Efficiency, *ACS Appl. Mater. Inter.,* 2015, **7**(31), 17138-17154.

10 A. Serr` a, R. Artal, J. García-Amor´ os, E. G´ omez, L. Philippe, Circular zero-residue process using microalgae for efficient water decontamination, biofuel production, and carbon dioxide fixation, *Chem. Eng. J.,* 2020, **388**, 124278.

11 H. Qin, H. Cheng, H. Li, Y. Wang, Degradation of ofloxacin, amoxicillin and tetracycline antibiotics using magnetic core–shell $MnFe_2O_4$@C-NH_2 as a heterogeneous Fenton catalyst, *Chem. Eng. J.,* 2020, **396**, 125304.

12 J. Liu, K Luo, X. M. Li, Q. Yang, D. B. Wang, Y. Wu, Z. Chen, X. D. Huang, Z. J. Pi, W. J. Du, Z. L. Guan, The biochar-supported iron-copper bimetallic composite activating oxygen system for simultaneous adsorption and degradation of tetracycline, *Chem. Eng. J.,* 2020, **402**, 12603.

13 H. Zhang, Y. Y. Song, L. C. Nengzi, J. F. Gou, B. Li, X. W. Cheng, Activation of persulfate by a novel magnetic $CuFe_2O_4/Bi_2O_3$ composite for lomefloxacin degradation, *Chem. Eng. J.,* 2020, **379**, 122362.

14 X. L. Zhu, H. H. Miao, J. Z. Chen, X. W. Zhu, J. J. Yi, Z. Mo, H. M. Li, Z. K. Zheng, B. B. Huang and H. Xu, Facet-dependent CdS/Bi_4TaO_8Cl Z-scheme heterojunction for enhanced photocatalytic tetracycline hydrochloride degradation and the carrier separation mechanism study via single-particle spectroscopy, *Inorg. Chem. Front.,* 2022, **9**, 2252-2263.

15 S. J. Li, M. J. Cai, Y. P. Liu, J. L. Zhang, C. C. Wang, S. H. Zang, Y. J. Li, P. Zhang and X. Li, In situ construction of a C_3N_5 nanosheet/Bi_2WO_6 nanodot S-scheme heterojunction with enhanced structural defects for the efficient photocatalytic removal of tetracycline and Cr(VI), *Inorg. Chem. Front.,* 2022, **9**, 2479-2497.

16 A. Wang, Z. K. Zheng, H. Wang, Y. W. Chen, C. H. Luo, D. J. Liang, B. Hu, R. L. Qiu, K. Yan, 3D hierarchical H_2-reduced Mn-doped CeO_2 microflowers assembled from nanotubes as a high-performance Fenton-like photocatalyst for tetracycline antibiotics degradation, *Appl. Catal. B: Environ.,* 2020, **277**, 119171.

17 H. C. Shan, D. Cai, X. X. Zhang, Q. Zhu, P. Y. Qin, J. Baeyens, Donor-acceptor type two-dimensional porphyrin-based covalent organic framework for visible-light-driven heterogeneous photocatalysis, *Chem. Eng. J.,* 2022, **432**, 134288.

18 G. T. Zan, T. Wu, F. Zhu, P. F. He, Y. P. Cheng, S. S. Chai, Y. Wang, X. F. Huang, W. X. Zhang, Y. Wan, X. J. Peng, Q. S. Wu, A Biomimetic Conductive Super-foldable Material, *Matter.,* 2021, **4**(10): 3232-3247.

19 S. S. Chai, G. T. Zan, K. Z. Dong, T. Wu, Q. S. Wu, Approaching Superfoldable Thickness-Limit Carbon Nanofiber Membranes Transformed From Water-Soluble PVA, *Nano Lett.*, 2021, **21**, 8831-8838.

20 Z. F. Yang, X. N. Xia, L. H. Shao, L. L. wang, Y. T. Liu, Efficient photocatalytic degradation of tetracycline under visible light by Z-scheme Ag_3PO_4/mixed-valence MIL-88A(Fe) heterojunctions: Mechanism insight, degradation pathways and DFT calculation, *Chem. Eng. J.,* 2021, **410**, 128454.

21 Y. Y. Liu, X. J. Wang, Q. N. Sun, M. Yuan, Z. H. Sun, S. Q. Xia, J. F. Zhao, Enhanced visible light photo-Fenton-like degradation of tetracyclines by expanded perlite supported $FeMo_3O_x$/g-C_3N_4 floating Z-scheme catalyst, *J. Hazard. Mater.,* 2022, **424**, 127387.

22 G. T. Zan, T. Wu, Z. L. Zhang, J. Li, J. C. Zhou, F. Zhu, H. X. Chen, M. Wen, Xiuchun Yang, Xiaojun Peng, Jun Chen, Qingsheng Wu, Bioinspired Nanocomposites with Self-adaptive Stress Dispersion for Super-Foldable Electrodes, *Adv. Sci.,* 2022, **9**(3), 2103714.

23 G. T. Zan, T. Wu, W. Y. Dong, J. C. Zhou, T. Tu, R. X. Xu, Y. Chen, Y. Wang, Q. S. Wu, Two-Level Biomimetic Designs Enable Intelligent Stress Dispersion for Super-Foldable C/NiS Nanofiber Free-Standing Electrode, *Advanced Fiber Materials*, 2022, **4**, 1177-1190.

24 R. Hailili, Z. Q. Wang, X. Q. Gong, C. Y. Wang. Oxygen vacancies induced visible-light photocatalytic activities of $CaCu_3Ti_4O_{12}$ with controllable morphologies for antibiotic degradation, *Appl. Catal. B: Environ.,* 2018, **221**, 422-432.

25 L. Fu, W. Zhou, M. Wen, D. D. Wu. Layered CuNi-Cu_2O/$NiAlO_x$ nanocatalyst for rapid conversion of p-nitrophenol to p-aminophenol, *Nano Res.*, 2021, **14**(12), 4616-4624.

26 F. Wu, S. Banerjee, H. F. Li, Y. Myung, P. Banerjee, Indirect Phase Transformation of CuO to Cu_2O on a Nanowire Surface, *Langmuir,* 2016, **32**, 4485-4493.

27 A. I. Kontos, V. Likodimos, T. Stergiopoulos, D. S. Tsoukleris, P. Falaras, Self-Organized Anodic TiO_2 Nanotube Arrays Functionalized by Iron Oxide Nanoparticles, *Chem. Mater.,* 2009, **21**, 662-672.
28 T. Vandhana, A.J. C. Lourduraj, Biogenic synthesis of Mn-Ag co-doped FeO ($Fe_{1-2x}Mn_xAg_x$) nanoparticles: As an effective disinfectant and anticancer agent, *Inorg. Chem. Commun.,* 2020, **112**, 107712.
29 H. Naatz, S. Lin, R. B. Li, W. Jiang, Z. X. Ji, C. H. Chang, J. Koser, T. Xia, A. E. Nel, L. Madler, and S. Pokhrel, Safe-by-Design CuO Nanoparticles via Fe-Doping, Cu–O Bond Length Variation, and Biological Assessment in Cells and Zebrafish Embryos, *ACS Nano,* 2017, **11**, 501-515.
30 L. Zhang, Y. Nie, C. Hu, J. Qu, Enhanced Fenton degradation of Rhodamine B over nanoscaled Cu-doped $LaTiO_3$ perovskite, *Appl. Catal. B: Environ.,* 2012, **125**, 418-424.
31 Y. Wang, H. Zhao, G. Zhao, Iron-copper bimetallic nanoparticles embedded within ordered mesoporous carbon as effective and stable heterogeneous Fenton catalyst for the degradation of organic contaminants, *Appl. Catal. B: Environ.,* 2015, **164**, 396-406.
32 X. Dong, B. Ren, Z. Sun, C. Li, X. Zhang, M. Kong, S. Zheng, D.D. Dionysiou, Monodispersed $CuFe_2O_4$ nanoparticles anchored on natural kaolinite as highly efficient peroxymonosulfate catalyst for Bisphenol A degradation, *Appl. Catal. B: Environ.,* 2019, **253**, 206-217.
33 X. Zhang, Y. Ding, H. Tang, X. Han, L. Zhu, N. Wang, Degradation of bisphenol A by hydrogen peroxide activated with $CuFeO_2$ microparticles as a heterogeneous Fenton-like catalyst: Efficiency, stability and mechanism, *Chem. Eng. J.,* 2014, **236**, 251-262.
34 J. Zhou, F. Ma, H. Guo, D. Su, Activate hydrogen peroxide for efficient tetracycline degradation via a facile assembled carbon-based composite: Synergism of powdered activated carbon and ferroferric oxide nanocatalyst, *Appl. Catal. B: Environ.,* 2020, **269**, 118784.
35 S. Chen, L. Tang, H. Feng, Y. Zhou, G. Zeng, Y. Lu, J. Yu, X. Ren, B. Peng, X. Liu, Carbon felt cathodes for electro-Fenton process to remove tetracycline via synergistic adsorption and degradation, *Sci. Total Environ.*, 2019, **670**, 921-931
36 H. Zheng, J. Bao, Y. Huang, L. Xiang, B. Faheem, J. Ren, M.N. Du, D.D. D. Nadagouda, Efficient degradation of atrazine with porous sulfurized Fe_2O_3 as catalyst for peroxymonosulfate activation, *Appl. Catal. B: Environ.*, 2019, **259**, 118056.
37 W Zhou, L Fu, L Zhao, X Xu, W Li, M Wen and Q Wu, Novel Core–Sheath Cu/Cu_2O-ZnO-Fe_3O_4 Nanocomposites with High-Efficiency Chlorine-Resistant Bacteria Sterilization and Trichloroacetic Acid Degradation Performance, *ACS Appl. Mater. Inter.*, 2021, **13**, 10878-10890.
38 X. F. Wei, H. Feng, L. W. Li , J. B. Gong, K. Jiang, S. L. Xue, P. K. Chu, Synthesis of tetragonal prismatic γ-In_2Se_3 nanostructures with predominantly {110} facets and photocatalytic degradation of tetracycline, *Appl. Catal. B: Environ.*, 2020, **260**, 118218.
39 S. Adhikari, S. Mandal, D.H. Kim, Z-scheme 2D/1D MoS_2 nanosheet-decorated $Ag_2Mo_2O_7$ microrods for efficient catalytic oxidation of levofloxacin, *Chem. Eng. J.*, 2019, **373**, 31-43.
40 S. Adhikari, H.H. Lee, D.H. Kim, Efficient visible-light induced electron-transfer in Z-scheme $MoO_3/Ag/C_3N_4$ for excellent photocatalytic removal of antibiotics of both ofloxacin and tetracycline, *Chem. Eng. J.*, 2020, **391**, 123504.
41 B. Wang, J. Di, P. Zhang, J. Xia, S. Dai, H. Li, Ionic liquid-induced strategy for porous perovskite-like $PbBiO_2Br$ photocatalysts with enhanced photocatalytic activity and mechanism insight, *Appl. Catal. B: Environ.*, 2017, **206**, 127-135.
42 A. Wang, Z. Chen, Z. Zheng, H. Xu, H. Wang, K. Hu, K. Yan, Remarkably enhanced sulfate radical-based photo-Fenton-like degradation of levofloxacin using the reduced mesoporous MnO@MnO_x microspheres, *Chem. Eng. J.*, 2020, **379**, 122340.
43 Z. Xie, Y. Feng, F. Wang, D. Chen, Q. Zhang, Y. Zeng, W. Lv, G. Liu, Construction of carbon dots modified MoO_3/g-C_3N_4 Z-scheme photocatalyst with enhanced visible light photocatalytic activity for the degradation of tetracycline, *Appl. Catal. B: Environ.*, 2018, **229**, 96-104.